Surface Morphology of Nimonic Alloy 263™ in Nanosecond Pulsed Laser Ablation

Zhehao Jiang, Sunil Pathak, S. Subramani, J. Radhakrishnan, and Sundar Marimuthu

Abbreviations

CPA	Chirped Pulse Amplification
DLW	Direct laser writing
EDM	Electrical Discharge Machining
FWHM	Full width Half Maximum
HAZ	Heat Affected Zone
LBM	Laser Beam Machining
LIP	Laser Induced Plasma
MOPA	Master Oscillator Power Amplifier
MRR	Material Removal Rate
Nd:YAG	Neodymium-doped Yttrium Aluminium Garnet

Z. Jiang
Loughborough University, Loughborough, UK

S. Pathak
Hilase Centre, Institute of Physics, Academy of Sciences of the Czech Republic, Za Radnici 828, 25241 Dolni Brezany, Czech Republic

S. Subramani
Department of Inorganic Chemistry, University of Chemistry and Technology Prague, Technick´a 5, 166 28 Prague 6, Czech Republic

J. Radhakrishnan (✉)
UPM Laser Centre, Universidad Politécnica de Madrid, 28031 Madrid, Spain
e-mail: r.jagdheesh@upm.es

S. Marimuthu
The Manufacturing Technology Centre, Ansty Business Park, Coventry, UK

Z. Jiang
Zhehao Jiang presently working at BSH Electrical Appliances Co., Ltd Nanjing, Nanjing, Jiangsu, People's Republic of China

PLA   Pulse Laser Ablation
SEM   Scanning Electron Microscope
Yb:YAG   Ytterbium-doped Yttrium Aluminium Garnet

1   Introduction

Precision machining of ultra-hard materials and superalloys are the prime limitations of conventional tool machining [1, 2]. Moreover, direct tool contact could ascend the mechanical stress load and probably change the alloy microstructure [2]. Nimonic Alloy 263™ is a class of nickel-based superalloys with extraordinary characteristics in excellent thermal conductivity, superb mechanical strength, and remarkable rust resistance, used in the rigorous operating conditions in gas turbine engines [3, 4]. Hence, it was recognized that advanced machining processes are expected to be developed under this age background. Nowadays, various non-contact based fabrication techniques have been more and more mature, including electrochemical machining (ECM), abrasive jet machining (AJM), and electrical discharge machining (EDM), ion beam micromachining (IBMM), and laser beam machining and micromachining (LBM, LMM) and so forth [4].

Laser beam machining (LBM) is a widely used advanced machining process, especially popular in welding, cutting, drilling, and hardening metallic sheets [4, 5]. Laser Beam Machining (LBM) is a machining method that uses a laser beam to engrave metallic and non-metallic materials. In this technique, a high-intensity laser beam is directed towards the workpiece, and the laser's thermal energy is transmitted to the workpiece's surface (workpiece). The heat generated at the surface warms, melts, and vaporizes the w/p components [5]. LBM, in general, is concerned with machining and material processing such as heat treatment, alloying, cladding, sheet metal bending, and so on. This type of processing uses the energy of coherent photons or laser beams, which are mostly transformed into thermal energy when they contact most materials. Moreover, the lasers are now used in regenerative machining and fast prototyping and procedures like stereolithography and selective laser melting [6].

Usually, continuous waved lasers are suitable for metallic sheet welding and hardening, which should attribute to its constant average power output. In contrast, rather than continuous waved lasers, pulsed lasers are used in deep penetration applications due to their intense power density. Pulsed lasers used for applications can be divided into millisecond (ms), microsecond (μs), nanosecond (ns), picoseconds (ps), and femtoseconds (fs) those five categories up to their pulse durations [6–8]. In order to recycle costly advanced engineering materials like Nimonic Alloy 263™, pulsed laser ranges from short pulse (ms-ns) to ultrashort pulse (ps-fs) are used in ablating material surface coating or cracked surface substrate layer. For pulsed laser ablation, the photon substrate interaction mechanism goes through heating, melting, boiling, and vaporization these four periods with an increase of power density [9]. It has been very well researched [10–12] that a higher material removal rate can be achieved in

the high power density that laser beam can penetrate deeper in the targeted irradiated area. Jeong et al. [13] and Palanco et al. [14] observed that a large amount of ionized ejected material could transfer into plasma plume, absorbing the consecutive laser energy and restricting the following: ablation. The higher power density applied i.e., over a saturation point 4–5×10^8 W/cm^2 may lead to a more obvious plasma shielding effect; it would be found when the power density is over a saturation point. In recent years, ultrashort UV laser ablation has become acclaimed because of its high power density that can alter material ejection mechanism from explosive melt dominated to vaporization dominated while descending plasma shield effect [15]. Once the pulse duration is no longer than the picosecond regime, the ablation process does not induce a melting process because there is less interaction time available for thermal diffusion via heat conduction. Compared to short-pulse laser ablation, undesirable heat effects on the valuable substrate in the form of micro-cracks, recast layer, and HAZ can be greatly minimized via material vaporization [16, 17]. Nevertheless, high operating costs and complex setup are the significant issues restricting its application scope.

Recently, a new fibre-based amplifier technology (MOPA) in a few ns pulse duration instead of chirped Pulse Amplification (CPA) ultrashort pulse in several ps or fs regimes was developed in balancing cost and ablation performance [18]. Compared to the traditional Q-switched fibre laser, MOPA fibre laser uses controllable pulse durations separately in each pass, meaning quality and efficiency can be achieved simultaneously through rough-based high material removal at premiere scanning and precisely based low material removal at post scanning [19]. Unlike peak power significantly reduced with increased laser frequency in Q-switched laser, limited peak power reduction by using higher frequency MOPA fibre laser [20].

In this chapter, a univariate experiment in changing a single parameter while keeping others constant is used to explore process parameters including pulse duration, frequency, power density, and scanning speed effects on MOPA ns fibre laser ablation Nimonic Alloy 263™. The optimum value of each parameter could be filtered out after parametric analysis according to the performance on ablation depth or surface roughness.

2 Materials and Methods

In the present work, an SPI MOPA pulsed fibre laser with wavelength 1.06 μm, FWHM pulse duration from 19 to 46 ns with frequency ranges from 1 to 1000 kHz was used as the power source. A moving direct laser writing (DLW) galvo scanner worked on Nimonic Alloy 263™ samples of dimension 75(L) × 15(W) × 2(T) mm in scanning speed up to 100 mm/s was used in the present experimentation. The details of the levels of parameters used in the experiment are shown in Table 1.

The scanner head is fitted with an F-Theta lens with a focal position to the top of the workstation, 178 mm (176 mm + 2 mm mild steel base). Due to the high thermal conductivity of Nimonic Alloy 263™, high laser power density could lead to substrate sheet deformation, shown in Fig. 1a. The 2 mm mild steel base was

**Table 1** Parameters and levels use for experimentation

S.no	Optimum frequency (kHz)	Pulse duration (ns)	Peak power (kW)	Speed (mm/s)
1	70	46	13	1
2	70	46	13	5
3	70	46	13	10
4	70	46	13	20
5	70	46	13	50
6	70	46	13	80
7	158	37	11	1
8	158	37	11	5
9	158	37	11	10
10	158	37	11	20
11	158	37	11	50
12	158	37	11	80
13	350	23	10	1
14	350	23	10	5
15	350	23	10	10
16	350	23	10	20
17	350	23	10	50
18	350	23	10	80

clamped below the targeted substrate to minimize the residual heat effect. For the fair thermal conductivity of mild steel, partial heat can be shared by the mild steel base; thus, the severity of deformation can greatly descend, shown in Fig. 1b. The laser beam scanned 15 mm in lines varying with speed change in the longitudinal width direction, and the intermediate section was chosen to avoid the acceleration effect. Spot diameter was estimated to the spot size of the ablation removal threshold by the method provided by Liu (1982) and theoretically calculated refer to Eq. (1) [18].

$$d = 2.44 \frac{f\lambda}{D} \tag{1}$$

where d is the spot diameter, f is the focal length, λ is the wavelength, and D is the beam diameter. The spot diameter was calculated to be 32 μm.

Precise control of lens-to-substrate distance at constant 178 mm was ensured to provide a stable spot diameter of 32 μm on the laser-substrate interaction zone. A 2 bar extractor was used to inhale ejected hazard in mid-air, and all experiment progress was performed without any assisted gas auxiliary. Eventually, optical and scanning electronic microscopes (SEM) was used to analyze ablated samples.
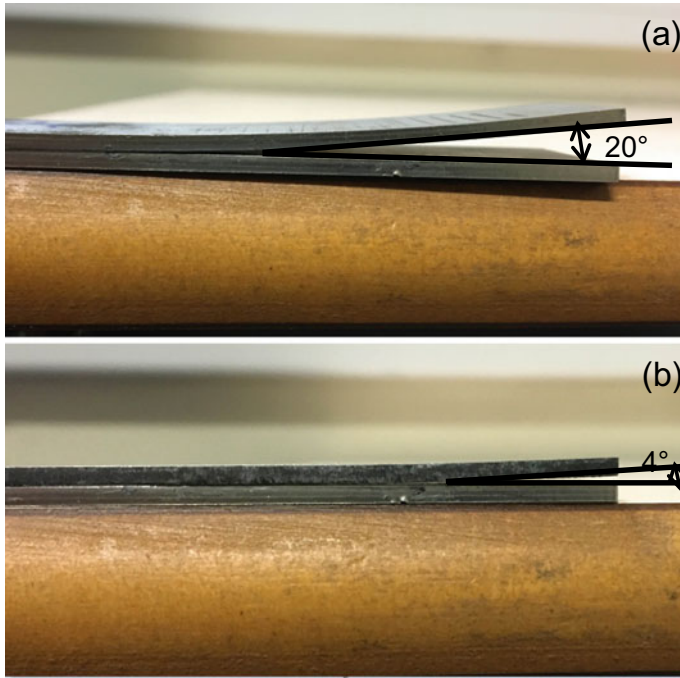
Fig. 1 Deformation comparison between **a** clamped without mild steel base, **b** clamped with mild steel base (Pulse duration = 46 ns, frequency = 70 kHz, power density = 16.2 × 10^5 kW/cm^2)

3   Results and Discussion

Referring to Eqs. (2) and (3), power output is determined by frequency and pulse duration.

$$P_{avg} = E \times f \tag{2}$$

And,

$$P_{peak} = \frac{E}{\Delta T} \tag{3}$$

Where P_{avg} is the average power, P_{peak} is the peak power, E is the pulse energy, and ΔT is the pulse duration.

According to synchronized consideration of the connection between each process parameter, so before exploring the effects of power density on laser ablation, the significance of researching the relationship among pulse duration, frequency, and ablation performance is noticeable.

## 3.1 Frequency Effects on Power Output

MOPA in the machine enables altering an extensive range of pulse duration, and a wide selection of corresponding optimum laser frequency ranges from 0 to 1000 kHz for different usage. Laser frequency represents the cycle time of one pulse shot, starting from one pulse to the beginning of the following pulse. Pulse duration delegates the duration of pulse-substrate interaction. Pulse duration is a phase of laser frequency without takt time. The optimum frequency at constant pulse duration can achieve the maximum output peak power, as shown in Fig. 2. In this diagram, the optimum frequency for laser FWHM pulse duration at 46 ns is 70 kHz, giving 100% peak power output. With the increase of laser frequency, the peak power output decreases, varying with it. Peak power output can be regulated via changing laser frequency for a particular laser pulse duration. Pulse duration will not be altered with the change of laser frequency, and there is no direct relationship between laser frequency and pulse duration.
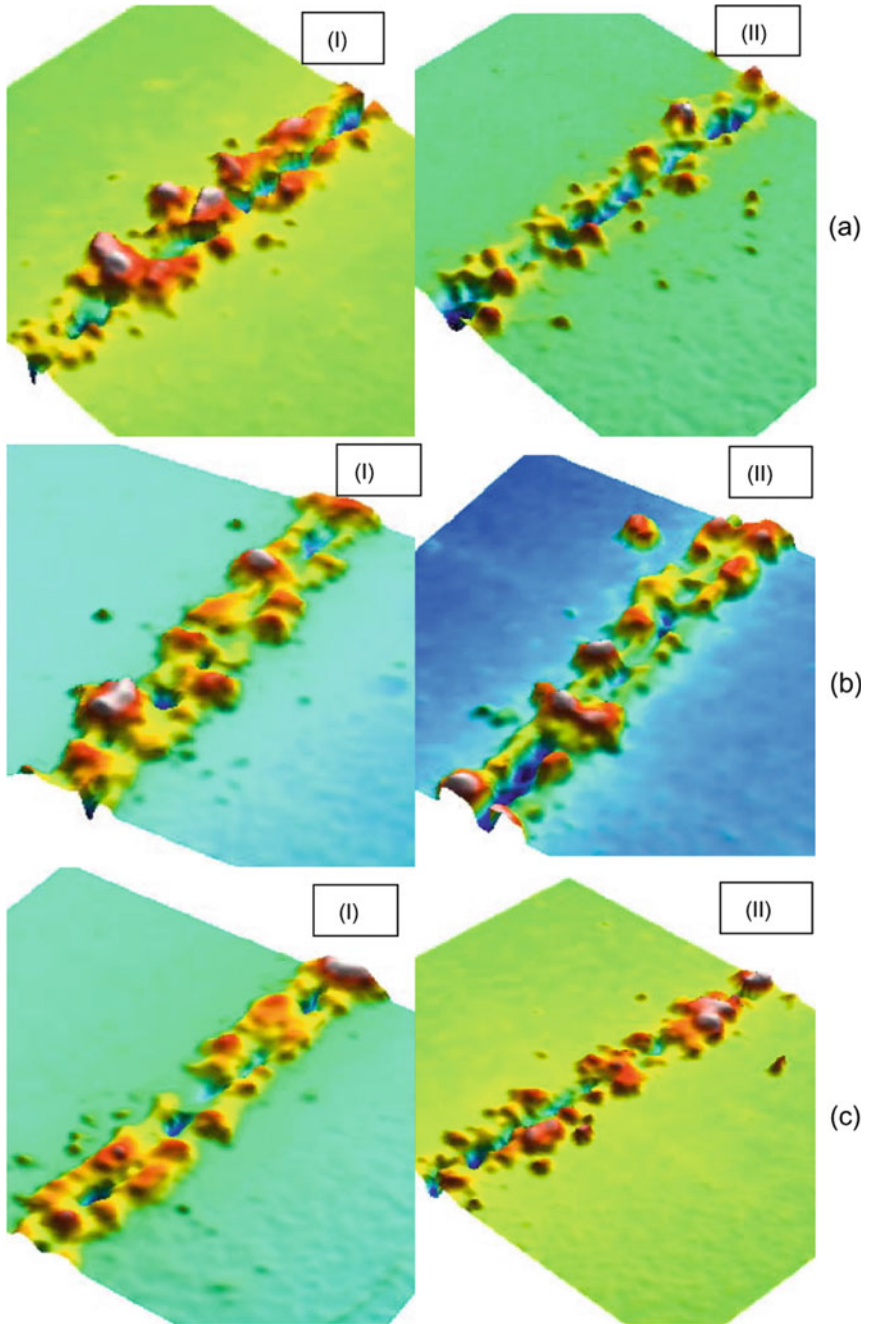
3.2 Pulse Duration Effects on Ablation Depth

When the pulse durations changed during the progress, the optimum frequency automatically varied with it. To identify the effects of pulse duration on ablation depth, three dispersed FWHM pulse duration parameters in scope range were selected (46 ns pulse duration with optimum frequency 70 kHz, 37 ns pulse duration with optimum frequency 158 kHz, and 23 ns pulse duration with optimum frequency 350 kHz).
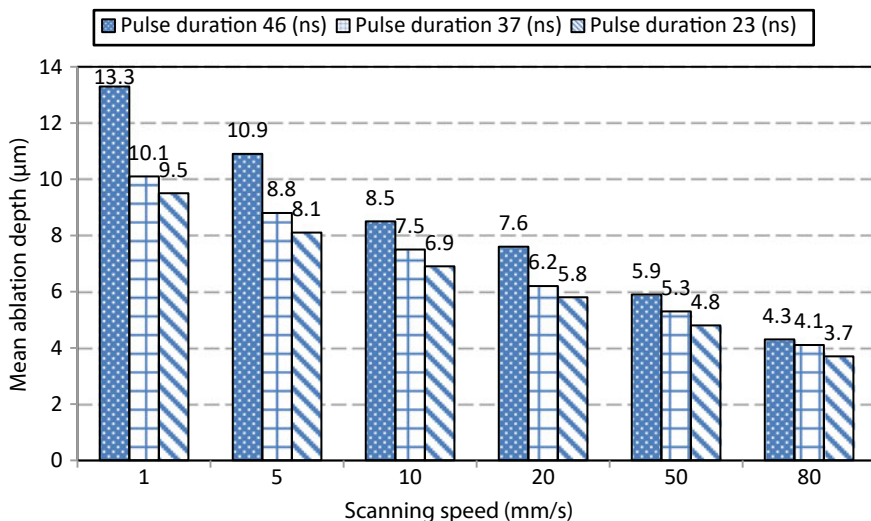
The ablation appearances of PLA on the flat nickel superalloy at one pass for selected pulse durations are shown in Fig. 3a 46 ns, (b) 37 ns, and (c) 23 ns at

Fig. 2 Diagram showing frequencies effect on peak power at FWHM pulse duration 46 ns
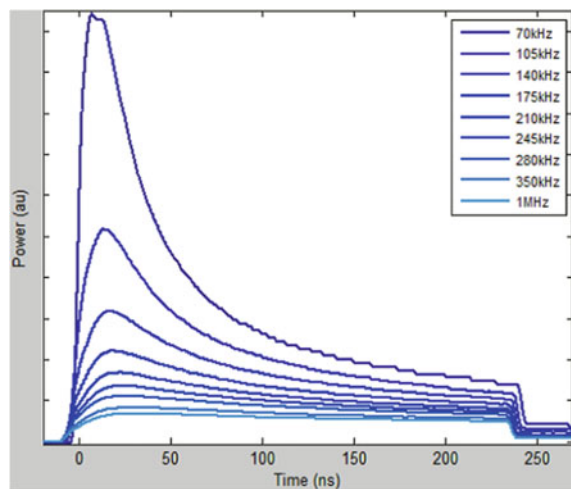
Fig. 3 Ablation appearance of different pulse durations **a** 46 ns, **b** 37 ns, and **c** 23 ns at different speed (I) 1 mm/s and (II) 50 mm/s

Fig. 4 Effect of pulse durations on mean ablation depth at maximum power output

two different speeds (I) 1 mm/s and (II) 50 mm/s. The optimum frequency gave the maximum peak power output, and respective were 13 kW, 11 kW, and 10 kW. As can be seen from the Figure, maximum peak power output led to a large amount of redeposited debris scattered alongside the ablation line, and higher scanning speed performed more obvious debris deposited phenomenon than lower speed. Mean ablation depth for the 18 sets of ablation lines is calculated and shown in Fig. 4.

From Fig. 4, it is evident that a higher pulse duration laser results in higher ablation depth due to longer effective laser-substrate interaction reaction and higher pulse peak power. Laser with pulse duration of 46 ns gave out a 13.3 µm mean ablation depth while other twos only had 10.1 µm and 9.5 µm at laser scanning speed 1 mm/s, respectively. Moreover, the mean ablation depth gradually decreases with increasing laser scanning speed in a decreasing exponential function trend. Laser pulse duration 46 ns with peak power 13 kW exhibited good ablation depth performance.

3.3 Power Density Effects on Ablation Performance

It is known that the plasma shield could be formed in a nanosecond laser regime when the laser power density is over 4–5×10^5 kW/ cm^2 [9, 13–15]. The calculation for power density can refer to Eq. (4).

$$F = \frac{P}{A} \tag{4}$$

Table 2 Calculations for the power density (kW/ cm^2)

S.No	Power percentage (%)	Peak power (kW)	Power density (kW/cm^2)
1	10	1.3	1.6×10^5
2	20	2.6	3.2×10^5
3	30	3.9	4.8×10^5
4	40	5.2	6.5×10^5
5	50	6.5	8.1×10^5
6	60	7.8	9.6×10^5
7	70	9.1	11.3×10^5
8	80	10.4	12.9×10^5
9	90	11.7	14.5×10^5
10	100	13.0	16.2×10^5

where F is power density (W/cm^2), P is laser power, and A is beam cross-sectional area.

The machine's effective beam cross-section spot diameter was 32 µm, so the effective beam cross-sectional area here was 8.04×10^{-6} cm^2. The calculation results for different power percentages are shown in Table 2.

All the ablation lines were applied to unify the speed parameter for a scanning speed of 4 mm/s. Top view of ablation lines under optical microscope at power density (a) 3.2×10^5 kW/cm^2, (b) 8.1×10^5 kW/cm^2 and (c) 14.5×10^5 kW/cm^2 are shown in Fig. 6 at the same magnification 10×. As shown in Fig. 5, with increasing power density, the melting zone became larger, and a more evident heat-affected edge along the longitudinal line direction can be seen. For power density 14.5×10^5 kW/cm^2, the melting pool diameter could reach 131.65 µm, whereas only 62.82 µm for power density 3.2×10^5 kW/cm^2. The appearances of ablation lines under using power density (a) 1.6×10^5 kW/cm^2, (b) 4.8×10^5 kW/cm^2, (c) 8.1×10^5 kW/cm^2 and (d) 14.5×10^5 kW/cm^2 are shown in Fig. 6.

As shown in Fig. 6, nearly no material removal happened when using power density 1.6×105 kW/cm^2, and with an enhancement of power density, material removal became manifest in the presence of debris deposited and ablation depth. The appearance of ablation lines under power density (c) 8.1×10^5 kW/cm^2 and (d) 14.5×10^5 kW/cm^2 look similar to others.

Figure 7a shows the captured laser-induced plasma flume working at scanning speed 4 mm/s with power density 12.9×10^5 kW/cm^2; it justifies that the plasma effect occurs when the laser power density reaches a specific value in MOPA ns fibre laser ablation. The mean ablation depth for all 10 set lines is analyzed in Fig. 7b. As illustrated in Fig. 7b, the ablation depth increases with laser power density in a positive linear correlation. The power density for the nickel superalloy ablation threshold is close to 1.6×10^5 kW/cm^2. The variation was amplified from 1.6×10^5 to 8.1×10^5 kW/cm^2 till it reached saturation point at power density 8.1×10^5 kW/cm^2. The power density over the saturation point was likely affected by the plasma shielding
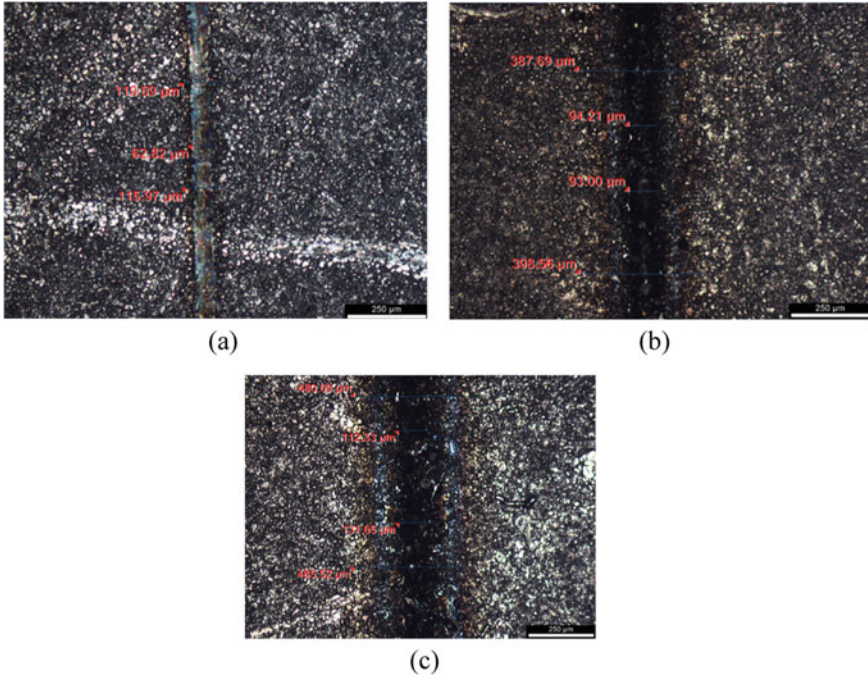
Fig. 5 Top view of ablation lines under optical microscope at power density at **a** 3.2×10^5 kW/cm², **b** 8.1×10^5 kW/cm² and **c** 14.5×10^5 kW/cm² (Scanning speed = 4 mm/s, pulse duration = 46 ns)

effect. The plasma cloud in the air absorbed the partial laser energy, and only specific energy could penetrate through the plasma cloud and strike on the substrate. The efficiency for laser irradiance was significantly discounted after penetrating the plasma shield, and with an increase of power density, the side effect of plasma became more apparent. The phenomenon is defined as Inverse Bremsstrahlung Absorption, a process of photons absorbed, scattered, and reflected by ionized gas electrons that lead to energy losses [12]. So power density at 8.1×10^5 kW/cm² with laser pulse duration is chosen due to its best cost performance on power usage and ablation efficiency. Power density at 8.1×10^5 kW/cm² corresponds to laser frequency 105 kHz at pulse duration 46 ns.

3.4 Scanning Speed Effects on Ablation Performance

Laser scanning speed is another pivotal process parameter that influences ablation performance. Veiko et al. [21] researched Q-switched ns fibre laser ablation of monocrystalline silicon and found that the laser ablation depth with increased scanning speed reflected a linear decline. Laser scanning speed effects on mean ablation
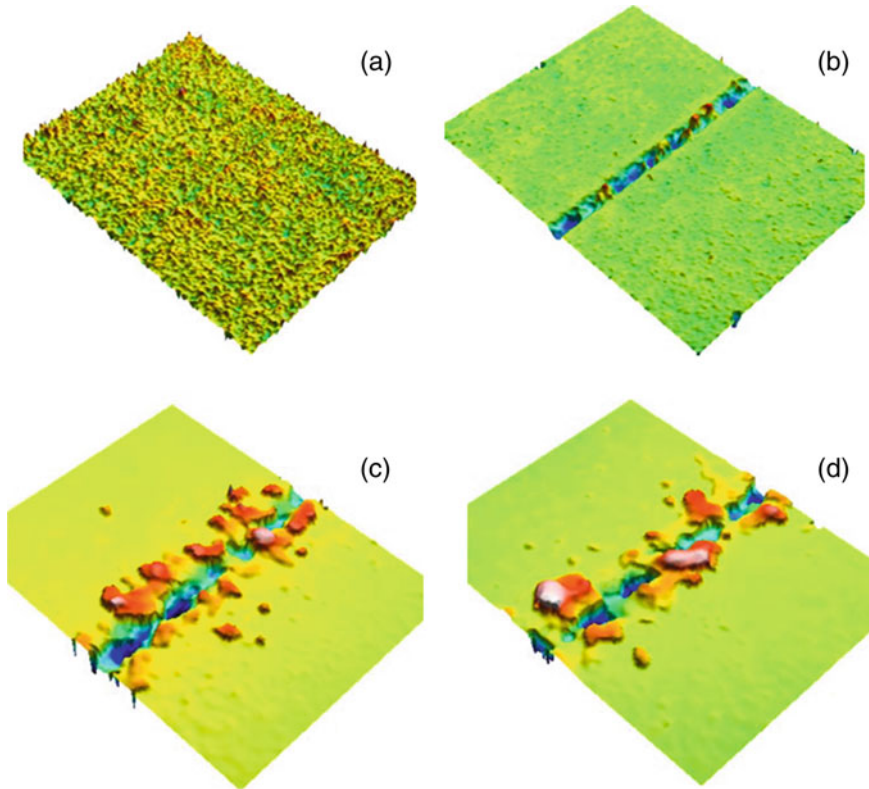
Fig. 6 Appearance of ablation lines at different power density **a** 1.6×10^5 kW/cm^2, **b** 4.8×10^5 kW/cm^2, **c** 8.1×10^5 kW/cm^2 and **d** 14.5×10^5 kW/cm^2 (Scanning speed = 4 mm/s, pulse duration = 46 ns)

depth and surface roughness are shown in Fig. 8a. Square markers in line represent scanning speed effects on surface roughness and values corresponding to the right side y-axis, while triangular markers in line represent scanning speed effects on mean ablation depth and values corresponding to the left side y-axis. The maximum value of mean ablation depth was 22.2 μm at speed 0.2 mm/s, and the minimum value was 2.8 μm at a speed of 100 mm/s.

Meanwhile, the maximum surface roughness value was 6.6 Ra at speed 0.2 mm/s, and the minimum value was 0.5 R_a at a speed of 100 mm/s. Unlike the linear relationship between scanning speed and mean ablation depth found in Q-switched ns fibre laser ablation, both curves show a decreasing exponential function trend with increasing scanning speed in the case of MOPA ns fibre laser ablation Nimonic Alloy 263™. It was found that an increase in scanning speed resulted in higher ablation depth whereas sacrifices surface finish to some extent.

Figure 8b reveals contour distribution of laser scanning speed on X–Y plane at laser pulse duration 46 ns with laser frequency 105 kHz applied in power density 8.1

(a)   (b)
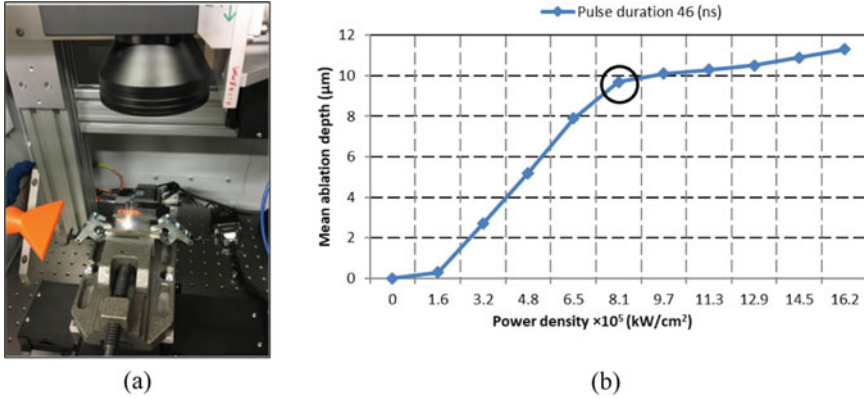
Fig. 7 **a** Laser induced plasma plume (Scanning speed = 4 mm/s, power density = 12.9 × 10^5 kW/cm^2); and **b** effects of power density on ablation depth of nickel super alloy (Pulse duration = 46 ns, scanning speed = 4 mm/s)

× 10^5 kW/cm^2 under PLA technique, which distinctly displays laser scanning speed effects on mean ablation depth and surface finish in the presence of contour density. The contour density gradually becomes sparse in the direction of arrow flow from higher speed to lower speed, which means one specific unit decrease in lower rate gives more sensitive effects on ablation efficiency.

Figure 9a,b reveal the SEM ablated line cross-section profile at scanning speeds 1 mm/s and 60 mm/s, respectively. The cross-section profiles reveal a 'V' shape in ablated grooves, and a large amount of the recast layer is re-solidified alongside the morphology, especially accumulated at the valley bottom in the light grey deep cone-shaped boundary before they were ejected by explosive melt ejection mechanism. Because low scanning speed led to higher pulses overlap, intensive laser pulse continuous shot on the melting pool, and the flux melting pool absorbed more laser energy in a unit area than high scanning speed did, which made ablation topology wider and deeper. With increasing of scanning speed from 1mms/s to 60 mm/s, the length of the recast layer decreased from 618 μm to 371 μm, and kerf width decreased from 105 μm to 67 μm. Meanwhile, a better surface finish at speed 60 mm/s than 1 mm/s in the presence of less spattered debris distributed around the rim. The hierarchy phenomenon of the recast layer shown in Fig. 9a can justify the unevenness of the ablation path. Barely any burnt HAZ was found after MOPA nanosecond fiber laser processing which should be attributed to the high thermal conductivity of Nimonic Alloy 263™.
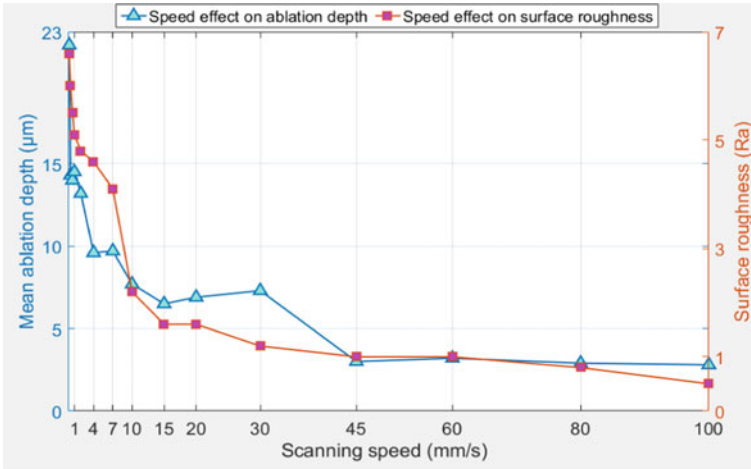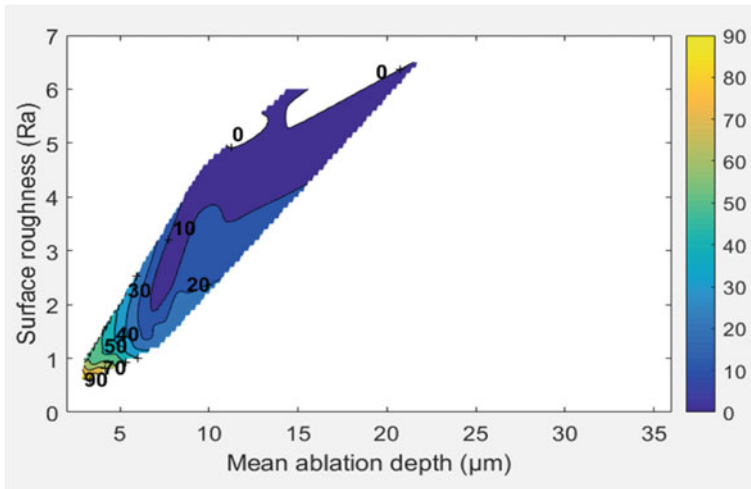
Fig. 8 Analysis of **a** laser scanning speed effects on ablation depth and surface roughness (Pulse duration = 46 ns, frequency = 105 kHz) and; **b** contour of laser scanning speed corresponds to X-axis mean ablation depth and Y-axis surface roughness (Pulse duration = 46 ns, frequency = 105 kHz, power density = 8.1 × 105 kW/cm^2)

4 Conclusion

The pilot experimental investigations were carried out to explore the effects of process parameters including pulse duration, frequency, power density, and laser scanning
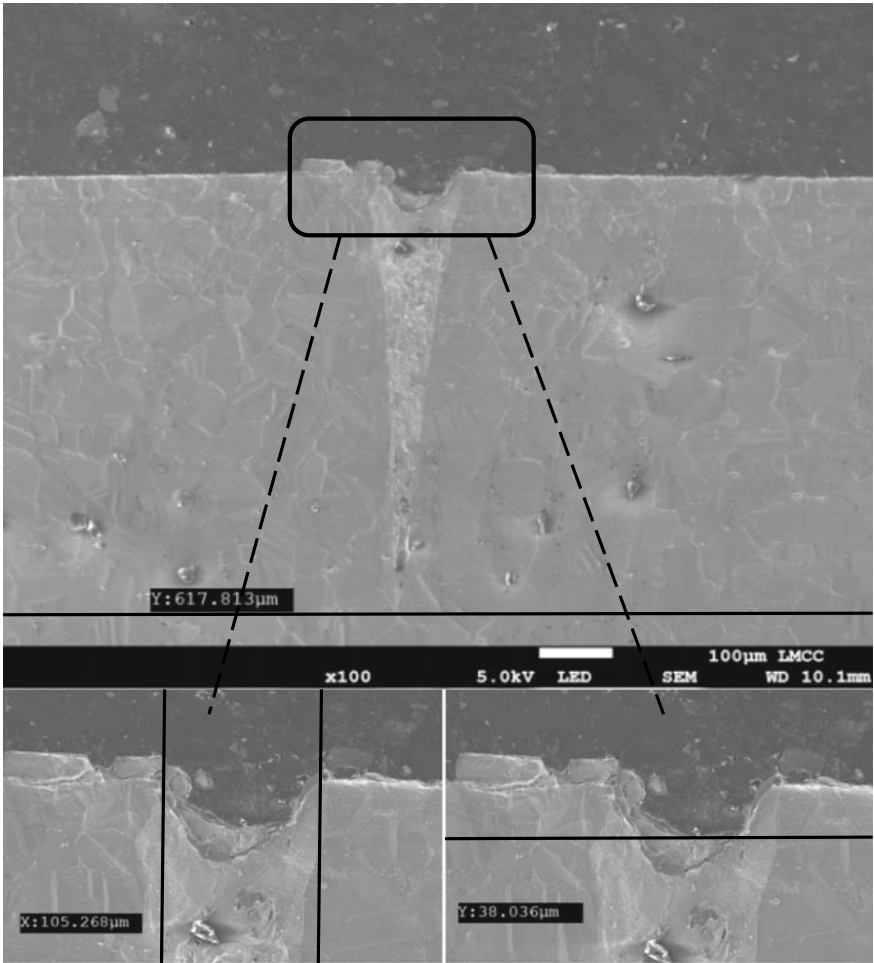
(a)

Fig. 9 Scanning electron microscopy images of **a** morphology of ablation line laser (Scanning speed = 1 mm/s, magnification 100×) and; **b** morphology of ablation line laser (Scanning speed = 60 mm/s, magnification 170×).

speed on high-frequency nanosecond pulsed laser ablation of Nimonic Alloy 263™. The following conclusions are drawn from the essence of the study.

- Nanosecond laser micromachining of Nimonic Alloy 263™ is recognized as an explosive melt ejection-dominated photo-thermal ablation.
- The optimum laser frequency corresponds to a specific laser pulse duration, giving out the maximum peak power in the MOPA laser generation system.
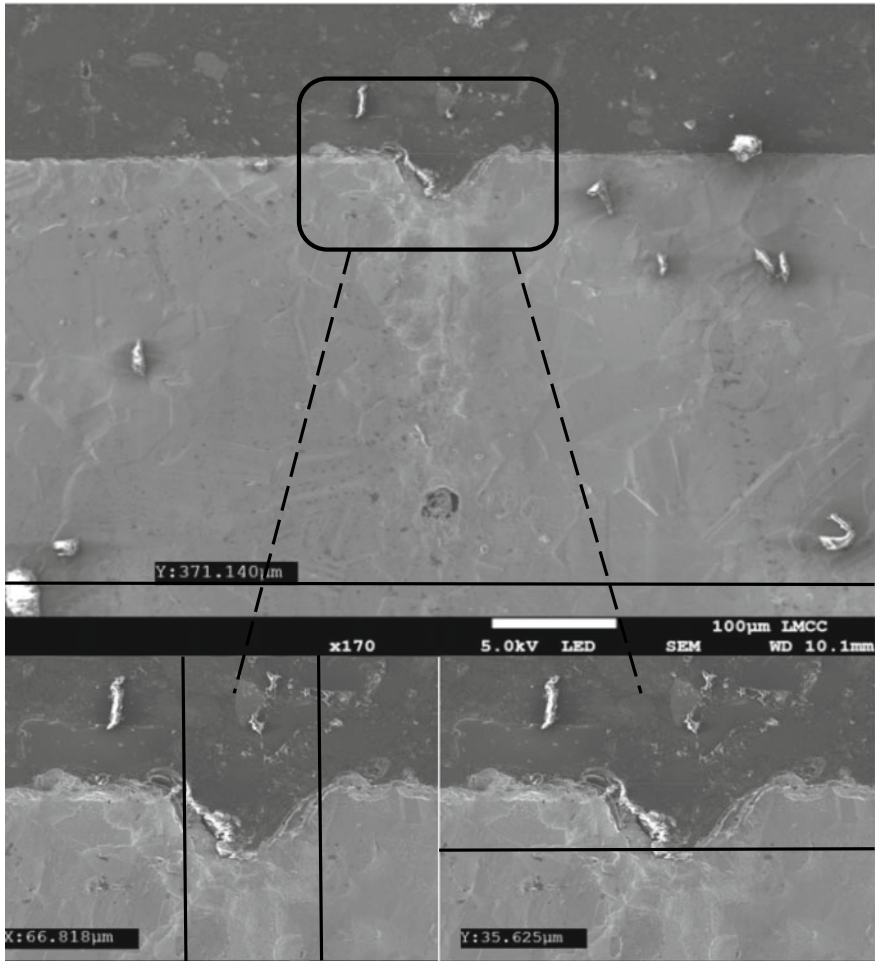
(b)

Fig. 9 (continued)

- An estimated 1.6×10^5 kW/cm^2 is the ablation threshold of the minimal material removal for the ejection mechanisms. With the increase of power density, ablation depth shared a linear ascend till the saturation point at power density 8.1×10^5 kW/cm^2.
- Laser-induced plasma cloud formed after power density reached 8.1×10^5 kW/cm^2. Plasma shield impeded the efficiency of natural laser energy ablating the Nimonic Alloy 263™ substrate.
- The 46 ns of pulse duration with laser frequency 105 kHz at power density 8.1×10^5 kW/cm^2 performed the optimum ablation in substrate penetrating.

- Increasing laser scanning speed leads to higher ablation depth whereas sacrifices surface finish to some extent.
- Few HAZ occurred after MOPA nanosecond fibre laser processing with optimum process parameters.

References

1. Pathak, S.: *Intelligent Manufacturing*. Springer Nature Switzerland AG (2021)
2. Zolpakar, N.A., Yasak, M.F., Pathak, S.: A review: use of evolutionary algorithm for optimisation of machining parameters. Int. J. Adv. Manuf. Technol. **115**, 31–47 (2021)
3. Kong, M.C., Wang, J.: Surface quality analysis of titanium and nickel-based alloys using Picosecond laser. Procedia CIRP **13**, 417–422 (2014)
4. Dubey, A.K., Yadava, V.: Laser beam machining—A review. Int. J. Mach. Tools Manuf **48**(6), 609–628 (2008)
5. Jagdheesh, R., Bičišťová, R., Brajer, J., Mocek, T.: Laser-induced superhydrophobic and oleophobic surface structures on float glass. Lasers Eng. **50**, 289–298 (2021)
6. Jagdheesh, R., Valarmathi, A., Sivakumar, M.: Influence of laser beam polarization on micromachining of crystalline silicon using ultrafast laser pulses. Lasers Eng. **32**, 19–35 (2021)
7. Jagdheesh, R., Kopecek, J., Brajer, J., Mocek, T.: Superhydrophobic microspiked surface structures by ultrashort laser patterning. Surf. Eng. **37**(10), 1266–1276 (2021). https://doi.org/10.1080/02670844.2021.1874651
8. Jagdheesh, R., Ocaña, J.L.: Laser machined ultralow water adhesion surface by low pressure processing. Mater. Lett. **270**, 127721 (2020). https://doi.org/10.1016/j.matlet.2020.127721
9. Jagdheesh, R., Tur, A., Ocaña, J.L.: The effects of pulse period on nanosecond laser microfabrication. Lasers Eng. **37**, 333–343 (2017)
10. Jagdheesh, R., Mudali, U.K., Nath, A.K.: Laser processed Cr–SiC coatings on AISI type 316L stainless steel. Surf. Eng. **23**, 93–98 (2007). https://doi.org/10.1179/174329407X169421
11. You, K., Yan, G., Luo, X., Gilchrist, M.D., Fang, F.: Advances in laser assisted machining of hard and brittle materials. J. Manuf. Process. **58**, 677–692 (2020)
12. Kaul, R., Ganesh, P., Sing, N., Jagdheesh, R., Bhagat, M.S., Kumar, H., Tiwari, P., Vora, H.S., Nath, A.K.: Effect of active flux addition on laser welding of austenitic stainless steel. Sci. Technol. Weld. Join. **12**, 127–137 (2007)
13. Petkov, P.V., Dimov, S.S., Minev, R.M., Pham, D.T.: Laser milling: Pulse duration effects on surface integrity. Proc. Inst Mech. Eng., Part B: J. Eng. Manuf. **222**(1), 35–45 (2008)
14. Shannon, M.A., Mao, X.L., Fernandez, A., Chan, W.-T., Russo, R.E.: Laser ablation mass removal versus incident power density during solid sampling for Inductively coupled plasma atomic emission spectroscopy. Anal. Chem. **67**(24), 4522–4529 (1995)
15. Horn, I., Guillong, M., Günther, D.: Wavelength dependant ablation rates for metals and silicate glasses using homogenized laser beam profiles—Implications for LA-ICP-MS. Appl. Surf. Sci. **182**(1–2), 91–102 (2001)
16. Vladiou, I., Stafe, M., Negutu, C., Popescu, I.M.: The dependence of the ablation rate of metals on nanosecond laser fluence and wavelength. J. Optoelectron. Adv. Mater. **10**(12), 3177–3181 (2008)
17. Jeong, S.H., Borisov, O.V., Yoo, J.H., Mao, X.L., Russo, R.E.: Effects of particle size distribution on Inductively coupled plasma mass Spectrometry signal density during laser ablation of glass samples. Anal. Chem. **71**(22), 5123–5130 (1999)
18. Palanco, S., Conesa, S., Laserna, J.J.: Analytical control of liquid steel in an induction melting furnace using a remote laser induced plasma spectrometer. J. Anal. At. Spectrom. **19**(4), 462 (2004)

19. Bogaerts, A., Chen, Z.: Effect of laser parameters on laser ablation and laser-induced plasma formation: a numerical modeling investigation. Spectrochim. Acta, Part B **60**(9–10), 1280–1307 (2005)
20. Penttilä, R., Pantsar, H., Laakso, P.: Picosecond Laser Processing—Material Removal Rates of Metals (2007). http://www.vtt.fi/files/research/ism/manufacturingsystems/nolamp_2007_picosencond_laser_processing.pdf. Accessed 8 May 2016
21. Lauer, B., Jäggi, B., Neuenschwander, B.: Influence of the pulse duration onto the material removal rate and machining quality for different types of steel. Phys. Procedia **56**, 963–972 (2014)